A Three-Dimensional Parabolic Equation Applied to VHF/UHF Propagation over Irregular Terrain

Chris A. Zelley, *Member, IEEE*, and Costas C. Constantinou, *Member, IEEE*

***Abstract*—The two-dimensional (2-D) parabolic equation (PE) is widely used for making radiowave propagation predictions in the troposphere. The effects of transverse terrain gradients, propagation around the sides of obstacles, and scattering from large obstacles to the side of the great circle path are not modeled, leading to prediction errors in many situations. In this paper, these errors are addressed by extending the 2-D PE to three dimensions. This changes the matrix form of the PE making it difficult to solve. A novel iterative solver technique, which is highly efficient and guaranteed to converge, is being presented. In order to confine the domain of computation, a three-dimensional (3-D) rectangular box is placed around the region of interest. A new second-order nonreflecting boundary condition is imposed on the surface of this box and its angular validity is established. The boundary condition is shown to keep unwanted fictitious reflections to an acceptable level in the domain of interest. The terrain boundary conditions for this 3-D PE method are developed and an original technique for incorporating them into the matrix form of the iterative solver is described. This is done using the concept of virtual field points below the ground. The prediction accuracy of the 3-D PE in comparison to the 2-D PE is tested both against indoor scaled frequency measurements and very high frequency (VHF) field trials.**

***Index Terms*— Mobile radio, parabolic equation, radiowave propagation, terrain.**

I. Introduction

THE parabolic equation (PE) models propagation of energy predominantly in one direction only. The field distribution on a plane transverse to the direction of propagation is "marched" forward in a step-by-step manner, provided the field is known on an initial plane. The field values at each step are calculated from the field values at the previous step. This is done subject to a radiation boundary condition at the top of the field plane and a terrain boundary condition at the bottom of this plane. Using this method, the shape and the electrical constants of the terrain can be accurately incorporated into the model. The majority of long-range propagation prediction methods in use are two-dimensional (2-D) and consider propagation along the great circle path between the transmitter and receiver [1]–[5]. However, when steep transverse terrain gradients exist along the great circle path or when the extent of horizontal Fresnel zone obstruction is comparable to the extent of vertical Fresnel zone obstruction, significant errors can occur. One of the strengths of the parabolic equation method is that it can readily model the effects of atmospheric refractive index gradients and absorption [6]. However, the work presented here was undertaken in order to develop a coverage prediction tool for short to medium ranges (up to 20 km) in the very high frequency (VHF) and ultrahigh frequency (UHF) bands for vehicle or man-portable equipment (i.e., ground- or near-ground-based antennas). For our purposes, experience shows that terrain effects are dominant over atmospheric effects and, therefore, the latter can be safely ignored. Thus, the inclusion of atmospheric refractivity is beyond the scope of this paper. Here, a three-dimensional (3-D) scalar PE code for free-space propagation over terrain has been developed, which makes use of a novel iterative solver technique to "march" a field plane though a 3-D region. A convergence criterion is established and convergence is formally proven for free-space propagation.

In order to restrict the 3-D PE computational domain, a rectangular box is placed around the area of interest. Nonreflecting boundary conditions (NRBC) are imposed on the surfaces of this box. A new nonreflecting boundary condition is derived and its accuracy examined. The boundary condition is then tested by propagating a Gaussian beam in free-space within a rectangular box and comparing the simulation predictions to the exact solution. A novel 3-D terrain boundary condition is incorporated into the 3-D PE scheme using the principle of virtual field points below the terrain, also presented here for the first time. An important limitation of this work that needs to be emphasised is that by restricting ourselves to a scalar field model, we are severely limited in modeling the depolarization effects of a general 3-D terrain. This introduces irreducible errors in our prediction capabilities which have been found not to be too severe.

Predictions made by the 3-D PE using the terrain boundary condition were then compared to propagation measurements made in both indoor and outdoor environments. The indoor measurements were made in the University of Birmingham indoor propagation range at 30 GHz and make use of the concept of scaled frequency modeling. These results clearly show the significant improvement in prediction accuracy that can be achieved using a 3-D model in a 3-D environment. Outdoor measurements were taken in the VHF and UHF bands at ranges up to 20 km. Examples of these along with 2-D PE and 3-D PE predictions are presented.

II. The 3-D Parabolic Equation

Assuming propagation to be predominantly along the z axis, the 3-D PE can be derived from the Helmholtz equation in

Manuscript received November 6, 1997; revised July 20, 1998. This work was supported by the EPSRC and DERA Malvern.

The authors are with the School of Electronic and Electrical Engineering, University of Birmingham, Edgbaston, Birmingham, B15 2TT U.K.

Publisher Item Identifier S 0018-926X(99)09390-4.

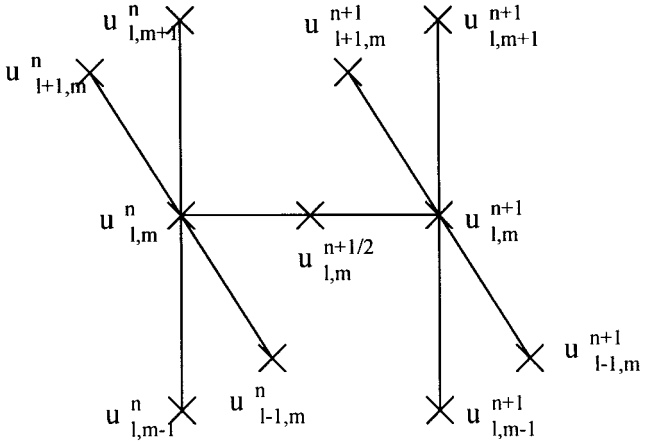

Fig. 1. Three-dimensional Crank–Nicholson scheme. Indexes l, m, and n correspond to discretized x, y, and z coordinates, respectively.

Cartesian coordinates by factoring out a fast varying phase term in the z direction. The refractive index term is assumed to be unity for the reasons explained in the introduction, giving

$$\frac{\partial u}{\partial z}(x,y,z) = \frac{j}{2k_0}\left(\frac{\partial^2}{\partial x^2} + \frac{\partial^2}{\partial y^2}\right)u(x,y,z). \tag{1}$$

This is the 3-D PE. The range of angles over which the 3-D PE is valid can be assessed by substituting a reduced plane wave solution into (1) and evaluating the error expression produced. The reduced plane wave solution is given by

$$u(x,y,z) = A\exp(jk_x x + jk_y y + jk_z z) \tag{2}$$

where

$$\begin{aligned} &k_x = k_0\sin\theta\sin\phi, \quad k_y = k_0\sin\theta\cos\phi \\ &k_z = k_0(\cos\theta - 1) \end{aligned} \tag{3}$$

and A is a constant amplitude term. The angle θ is the angle of propagation measured from the z axis and ϕ is the azimuth angle about the z axis. On substitution the ϕ terms can be eliminated to yield

$$e_{3\mathrm{DPE}} = 1 - \cos\theta - \frac{\sin^2\theta}{2}. \tag{4}$$

This is identical to the error expression of the 2-D PE. The 3-D PE is, therefore, accurate up to angles of $\pm 15°$ [7] for all angles ϕ. The relative error at $\theta = 15°$ is 0.000 58. The range of angles over which the 3-D PE is valid is dependent on the level of accuracy required by the user.

In order to solve the 3-D PE numerically, (1) can be expressed using finite differences. This is done using a 3-D version of the Crank–Nicholson scheme [8], [9]. In this scheme the 3-D PE is written using finite differences which are centered on a point midway between two successive planes of field points. A schematic diagram of the 3-D Crank–Nicholson scheme is shown in Fig. 1.

The first-order derivative with respect to z at the midpoint can be written as

$$\frac{\partial u}{\partial z}\left(n+\frac{1}{2}\right) = \frac{u_{l,m}^{n+1} - u_{l,m}^{n}}{\Delta z} + e_z\left(n+\frac{1}{2}\right) \tag{5}$$

where $e(n+\frac{1}{2})$ is the discretization error term. The second-order derivative with respect to x can be written as

$$\begin{aligned} &\frac{\partial^2 u}{\partial x^2}\left(n+\frac{1}{2}\right) \\ &\quad = \frac{u_{l,m-1}^{n+1} - 2u_{l,m}^{n+1} + u_{l,m+1}^{n+1}}{2\Delta x^2} \\ &\qquad + \frac{u_{l,m-1}^{n} - 2u_{l,m}^{n} + u_{l,m+1}^{n}}{2\Delta x^2} + e_x\left(n+\frac{1}{2}\right) \end{aligned} \tag{6}$$

and the second-order derivative with respect to y can be written as

$$\begin{aligned} &\frac{\partial^2 u}{\partial y^2}\left(n+\frac{1}{2}\right) \\ &\quad = \frac{u_{l-1,m}^{n+1} - 2u_{l,m}^{n+1} + u_{l+1,m}^{n+1}}{2\Delta y^2} \\ &\qquad + \frac{u_{l-1,m}^{n} - 2u_{l,m}^{n} + u_{l+1,m}^{n}}{2\Delta y^2} + e_y\left(n+\frac{1}{2}\right). \end{aligned} \tag{7}$$

The leading terms in the discretization errors are given by

$$e_z\left(n+\frac{1}{2}\right) = \frac{\Delta z^2}{24}\frac{\partial^3 u}{\partial z^3}\left(n+\frac{1}{2}\right) \tag{5a}$$

$$\begin{aligned} e_x\left(n+\frac{1}{2}\right) &= \frac{\Delta x^2}{12}\frac{\partial^4 u}{\partial x^4}\left(n+\frac{1}{2}\right) \\ &\quad + \frac{\Delta z^2}{8}\frac{\partial^2}{\partial x^2}\frac{\partial^2 u}{\partial z^2}\left(n+\frac{1}{2}\right) \end{aligned} \tag{6a}$$

$$\begin{aligned} e_y\left(n+\frac{1}{2}\right) &= \frac{\Delta y^2}{12}\frac{\partial^4 u}{\partial y^4}\left(n+\frac{1}{2}\right) \\ &\quad + \frac{\Delta z^2}{8}\frac{\partial^2}{\partial y^2}\frac{\partial^2 u}{\partial z^2}\left(n+\frac{1}{2}\right). \end{aligned} \tag{7a}$$

The derivatives (5)–(7) can be substituted into the 3-D PE (1), and this equation can then be rearranged such that the field points on the z_{n+1} plane are expressed in terms of the field points on the z_n plane

$$\begin{aligned} u_{l,m}^{n+1} &- \frac{j\Delta z}{4k_0}\left(\left(\frac{u_{l,m-1}^{n+1} - 2u_{l,m}^{n+1} + u_{l,m+1}^{n+1}}{\Delta x^2}\right)\right. \\ &\left. + \left(\frac{u_{l-1,m}^{n+1} - 2u_{l,m}^{n+1} + u_{l+1,m}^{n+1}}{\Delta y^2}\right)\right) \\ &= u_{l,m}^{n} + \frac{j\Delta z}{4k_0}\left(\left(\frac{u_{l,m-1}^{n} - 2u_{l,m}^{n} + u_{l,m+1}^{n}}{\Delta x^2}\right)\right. \\ &\left. + \left(\frac{u_{l-1,m}^{n} - 2u_{l,m}^{n} + u_{l+1,m}^{n}}{\Delta y^2}\right)\right). \end{aligned} \tag{8}$$

Expressing the 3-D PE using finite differences allows (8) to be cast into matrix form. The use of matrices permits the simultaneous calculation of field values over the entire field plane. The errors introduced by writing the 3-D PE using finite differences can be found by summing the error terms of (5a)–(7a). The size of the error can be controlled by the selection of the discretization intervals, Δx, Δy, and Δz. We have performed extensive numerical simulations for ranges up to $20\,000\lambda_0$ and for step sizes of $16\lambda_0$ in the z direction and up

to $2\lambda_0$ in the x–y plane, which reveal that the prediction error is well below 1 dB. However, we have established that the main contribution to the error is introduced by the boundary conditions discussed in the next section. Since the field plane is 2-D, the matrix equation can be expressed in the general form given by

$$\mathbf{A}\mathbf{U}^{n+1} + \mathbf{U}^{n+1}\mathbf{B} = \mathbf{D}\mathbf{U}^{n} + \mathbf{U}^{n}\mathbf{E} \tag{9}$$

where $\mathbf{U}^n$ and $\mathbf{U}^{n+1}$ are matrices describing field points on the n and $n+1$ field planes, respectively. The repeated solution of this equation allows the field distribution to be found over the entire region of interest, provided an initial field is known. $\mathbf{A}$, $\mathbf{B}$, $\mathbf{C}$, and $\mathbf{D}$ are square tridiagonal operator matrices given in

$$\mathbf{A} = \begin{bmatrix} X & \Gamma & 0 & \cdots & 0 & 0 \\ \Gamma & X & \Gamma & \cdots & 0 & 0 \\ & \cdot & \cdot & & & \\ & \cdot & \cdot & & & \\ 0 & 0 & 0 & \cdots & X & \Gamma \\ 0 & 0 & 0 & \cdots & \Gamma & X \end{bmatrix}$$

$$\mathbf{B} = \begin{bmatrix} V & I & 0 & \cdots & 0 & 0 \\ I & V & I & \cdots & 0 & 0 \\ & \cdot & \cdot & & & \\ & \cdot & \cdot & & & \\ 0 & 0 & 0 & \cdots & V & I \\ 0 & 0 & 0 & \cdots & I & V \end{bmatrix} \tag{10a}$$

$$\mathbf{D} = \begin{bmatrix} Y & H & 0 & \cdots & 0 & 0 \\ H & Y & H & \cdots & 0 & 0 \\ & \cdot & \cdot & & & \\ & \cdot & \cdot & & & \\ 0 & 0 & 0 & \cdots & Y & H \\ 0 & 0 & 0 & \cdots & H & Y \end{bmatrix}$$

$$\mathbf{E} = \begin{bmatrix} W & K & 0 & \cdots & 0 & 0 \\ K & W & K & \cdots & 0 & 0 \\ & \cdot & \cdot & & & \\ & \cdot & \cdot & & & \\ 0 & 0 & 0 & \cdots & W & K \\ 0 & 0 & 0 & \cdots & K & W \end{bmatrix} \tag{10b}$$

where

$$\begin{aligned} X &= 1 + \frac{j\Delta z}{2k_0\Delta x^2} \quad V = \frac{j\Delta z}{2k_0\Delta y^2} \\ Y &= 1 - \frac{j\Delta z}{2k_0\Delta x^2} \quad W = \frac{j\Delta z}{2k_0\Delta y^2} \\ \Gamma &= -\frac{j\Delta z}{4k_0\Delta x^2} \quad I = -\frac{j\Delta z}{4k_0\Delta y^2} \\ H &= \frac{j\Delta z}{4k_0\Delta x^2} \quad K = -\frac{j\Delta z}{4k_0\Delta y^2}. \end{aligned} \tag{11}$$

This facilitates the use of existing efficient tridiagonal linear equation solver routines. The right-hand side of the matrix equation (9) can be evaluated to give

$$\mathbf{A}\mathbf{U}^{n+1} + \mathbf{U}^{n+1}\mathbf{B} = \mathbf{C}. \tag{12}$$

However, this type of matrix equation is difficult to solve due to the presence of pre- and post-matrix multiplication. This means that (12) cannot be rearranged algebraically such that $\mathbf{U}^{n+1}$ can be expressed in terms of $\mathbf{A}$, $\mathbf{B}$ and $\mathbf{C}$. Previous 3-D PE methods have traditionally dealt with this problem by adopting an alternating direction implicit (ADI) marching method [6], [9]. This method effectively implements an equivalent 2-D marching step in the x–z plane, followed by an equivalent 2-D marching step in the y–z plane. This technique has been used extensively for underwater acoustic propagation where refractive effects are significant. However, for ground-based antennas on mountainous or hilly terrain, significant energy coupling on the sloping terrain boundary between the two transverse directions can occur within a single marching step. The ADI method would then result in the introduction of significant errors, thus the marching of the vertical and horizontal field planes must be done simultaneously.

An iterative equation is found by rearranging (12) to give

$$\mathbf{U}^{n+1}_{(i+1)} = \mathbf{A}^{-1}\mathbf{C} - \mathbf{A}^{-1}\mathbf{U}^{n+1}_{(i)}\mathbf{B}. \tag{13}$$

The use of tridiagonal matrices means that this equation can be solved efficiently. An iterative solver approach will only be useful provided that (13) converges rapidly. By using an initial estimate of the field at z_{n+1} plane and repeating the iteration N times, we arrive at

$$\begin{aligned} \mathbf{U}^{n+1}_{(N)} = &\sum_{i=1}^{N}[(-1)^{i-1}(\mathbf{A}^{-1})^{i-1}\mathbf{A}^{-1}\mathbf{C}(\mathbf{B})^{i-1}] \\ &+ (-1)^N(\mathbf{A}^{-1})^N\mathbf{U}^{n+1}_{(0)}(\mathbf{B})^N. \end{aligned} \tag{14}$$

For the iterative solver to converge, the field planes after N iterations must tend to a limiting spatial field distribution. This will occur provided that the two following conditions are met:

$$\lim_{N\to\infty}\left[(\mathbf{A}^{-1})^N\mathbf{U}^{n+1}_{(0)}(\mathbf{B})^N\right] \to \textit{Null Matrix} \tag{15}$$

$$\lim_{N\to\infty}[(\mathbf{A}^{-1})^N\mathbf{A}^{-1}\mathbf{C}(\mathbf{B})^N] \to \textit{Null Matrix}. \tag{16}$$

These conditions will be met provided that $(\mathbf{A}^{-1})^N$ and $(\mathbf{B})^N$ both tend toward the null matrix as N becomes large or if one of the terms tends toward the null matrix faster than the other term grows. This requires that the norm of matrices $\mathbf{A}^{-1}$ and $\mathbf{B}$ is as small as possible. To make the norm of $\mathbf{A}^{-1}$ as small as possible, the norm of $\mathbf{A}$ must be as large as possible. This must be done within the constraints of the 3-D PE in the Crank–Nicholson scheme. It is possible to transfer the leading diagonal terms from matrix $\mathbf{B}$ to matrix $\mathbf{A}$ without affecting the formulation of the 3-D PE. This has the effect of reducing the norm of matrix $\mathbf{B}$ while increasing the norm of matrix $\mathbf{A}$. The matrix terms for the 3-D PE now become

$$\begin{aligned} X &= 1 + \frac{j\Delta z}{2k_0\Delta x^2} + \frac{j\Delta z}{2k_0\Delta y^2} \quad V = 0 \\ \Gamma &= -\frac{j\Delta z}{4k_0\Delta x^2} \quad I = -\frac{j\Delta z}{4k_0\Delta y^2}. \end{aligned} \tag{17}$$

Taking these values and examining the effect of the iterative solver on an arbitrary field point within the field plane, convergence is guaranteed. This is done using the substitution of a reduced plane wave solution. Taking the finite-difference

equation (8), we can evaluate the right-hand side to give

$$u_{l,m}^{n+1} - \frac{j\Delta z}{4k_0}\left(\left(\frac{u_{l,m-1}^{n+1} - 2u_{l,m}^{n+1} + u_{l,m+1}^{n+1}}{\Delta x^2}\right) + \left(\frac{u_{l-1,m}^{n+1} - 2u_{l,m}^{n+1} + u_{l+1,m}^{n+1}}{\Delta y^2}\right)\right) = c_{l,m} \tag{18}$$

where $c_{l,m}$ is an arbitrary point in the $\mathbf{C}$ matrix of (12). Rearranging this equation in the form of the iterative solver that converges as discussed above we get

$$\left[u_{l,m}^{n+1} - \frac{j\Delta z}{4k_0}\left(\left(\frac{u_{l,m-1}^{n+1} - 2u_{l,m}^{n+1} + u_{l,m+1}^{n+1}}{\Delta x^2}\right) + \left(\frac{-2u_{l,m}^{n+1}}{\Delta y^2}\right)\right)\right]_{(i+1)} = c_{l,m} + \left[\frac{j\Delta z}{4k_0}\left(\frac{u_{l-1,m}^{n+1} + u_{l+1,m}^{n+1}}{\Delta y^2}\right)\right]_{(i)}. \tag{19}$$

Now using the substitution of the reduced plane wave solution of (2) we obtain

$$u_{(i+1)}\left[1 - \frac{j\Delta z}{4k_0}\left(\left(\frac{e^{-jk_x\Delta x} - 2 + e^{jk_x\Delta x}}{\Delta x^2}\right) + \left(\frac{-2}{\Delta y^2}\right)\right)\right] = c_{l,m} + u_{(i)}\left[\frac{j\Delta z}{4k_0}\left(\frac{e^{-jk_y\Delta y} + e^{jk_y\Delta y}}{\Delta y^2}\right)\right] \tag{20}$$

where the indexes l, m, and $n+1$ are implicitly assumed and are hereafter omitted for clarity. This leads to

$$u_{(i+1)}\left[1 - \frac{j\Delta z}{4k_0}\left(\left(\frac{2\cos(k_x\Delta x) - 2}{\Delta x^2}\right) + \left(\frac{-2}{\Delta y^2}\right)\right)\right] = c_{l,m} + u_{(i)}\left[\frac{j\Delta z}{4k_0}\left(\frac{2\cos(k_y\Delta y)}{\Delta y^2}\right)\right] \tag{21}$$

To find if this expression is convergent, we use the theory of fixed-point methods [10]. For (21) to converge, the inequality

$$\left|\frac{du_{(i+1)}}{du_{(i)}}\right| < 1 \tag{22}$$

must hold. Differentiating (21) we obtain

$$\frac{du_{(i+1)}}{du_{(i)}} = \frac{\left[\frac{j\Delta z}{4k_0}\left(\frac{2\cos(k_y\Delta y)}{\Delta y^2}\right)\right]}{\left[1 - \frac{j\Delta z}{4k_0}\left(\left(\frac{2\cos(k_x\Delta x) - 2}{\Delta x^2}\right) + \left(\frac{-2}{\Delta y^2}\right)\right)\right]}. \tag{23}$$

A small number of straightforward algebraic steps yields

$$\left|\frac{du_{(i+1)}}{du_{(i)}}\right| = \frac{\left(\frac{\Delta z}{2k_0\Delta y^2}\right)\left|\cos(k_y\Delta y)\right|}{\sqrt{1 + \left(\frac{\Delta z}{2k_0(\Delta y)^2}\right)^2\left[1 + 2\left(\frac{\Delta y}{\Delta x}\right)^2\sin^2\left(\frac{k_x\Delta x}{2}\right)\right]}}. \tag{24}$$

The worst case occurs when $\cos(k_y\Delta y) = \pm 1$ and $\sin(k_x\Delta x/2) = 0$ since the denominator is positive-definite, giving

$$\left|\frac{du_{(i+1)}}{du_{(i)}}\right| \leq \frac{\left[\frac{\Delta z}{2k_0\Delta y^2}\right]}{\sqrt{1 + \left[\frac{\Delta z}{2k_0\Delta y^2}\right]^2}} < 1. \tag{25}$$

It can be seen that the magnitude of the derivative is always less than unity irrespective of the discretization grid chosen. This means that convergence is guaranteed for an arbitrary plane wave. Performing the same analysis for a spectrum of plane waves will produce the same result. Selecting values of Δx, Δy, and Δz that make the numerical value of (24) significantly smaller than one guarantees faster convergence.

If the first convergence criterion given by (15) is satisfied, then the final solution given by (14) is independent of the initial estimate of the field at z_{n+1} plane. This means that the iterative solver technique will converge to the correct solution regardless of the initial estimate given. This is very useful since a bad initial estimate cannot lead to an incorrect result, although a bad initial estimate will require more iterations in order to converge. In this work the final solution at plane n has been used as the initial estimate of the field at plane $n+1$.

After each iteration step, a test for acceptable convergence is

$$\left\|\mathbf{U}_{(i+1)}^{n+1} - \mathbf{U}_{(i)}^{n+1}\right\| \leq e \tag{26}$$

where e is the maximum allowable norm of the error vector and can be chosen arbitrarily.

While (13) is satisfactory for propagation in free-space, it cannot be used when the boundary conditions around the field plane vary, as is the case for radiowave propagation over irregular terrain. This is due to the operator on each column of field points being dependent on the height, gradient, and surface impedance of the terrain below that column. To propagate a field solution forward in this situation we must generalize (13). To do this we replace matrix $\mathbf{A}$ with a number of matrices $\mathbf{A}_l$, each operating on the lth column in the matrix of field points $\mathbf{U}$ and, hence, providing the correct boundary conditions for each column (a column corresponds to a vertical column of field points). We similarly recast matrix $\mathbf{B}$ in this form to obtain

$$\{\mathbf{A}_1, \mathbf{A}_2, \cdots \mathbf{A}_l, \cdots \mathbf{A}_L\}\mathbf{U}^{n+1} + \mathbf{U}^{n+1}\{\mathbf{B}_1, \mathbf{B}_2, \cdots \mathbf{B}_m, \cdots \mathbf{B}_M\} = \mathbf{C} \tag{27}$$

which is written symbolically as

$$\{\mathbf{A}_l\}\mathbf{U}^{n+1} + \mathbf{U}^{n+1}\{\mathbf{B}_M\} = \mathbf{C}. \tag{28}$$

This generalized matrix equation can then be solved using the same iterative solver method described above. For the generalized iterative solver L matrix inversions must be performed at each iteration instead of a single inversion. We postpone any consideration of convergence and stability until the implementation of the boundary conditions has been discussed.

This generalized iterative solver has been implemented and used to solve a Crank–Nicholson implementation of a narrow angle 3-D PE. The ability of the iterative solver to converge rapidly is demonstrated by propagating a Gaussian beam of unity amplitude, with a $1/e$ beamwidth of 4.5° to a distance of 20 000 wavelengths. The cross section of the domain of interest measured $48\lambda_0 \times 48\lambda_0$. The second-order nonreflecting boundary condition presented in Section III of this paper was employed to bound the region of interest. The resolution and propagation stepsize defined by Nyquist sampling are $\Delta x = \Delta y = 2\lambda_0$ (due to the limitation of

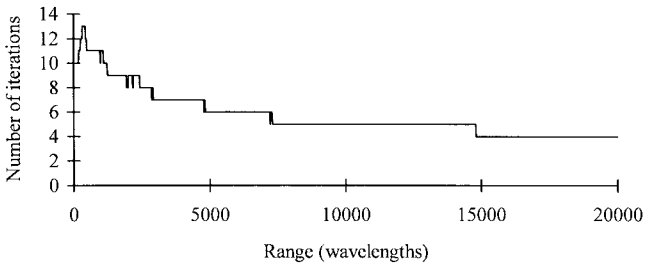

Fig. 2. Number of iterations required for convergence ($e \leq 0.000\,58$).

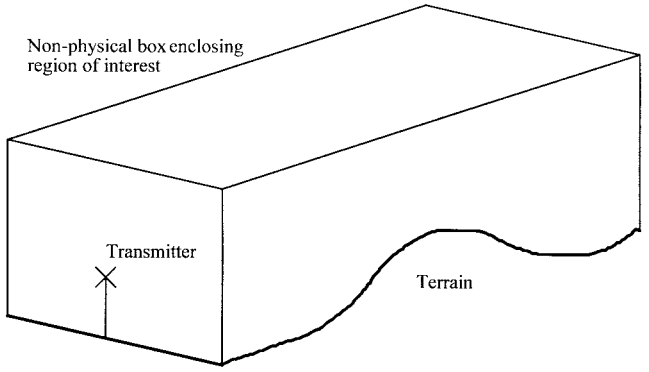

Fig. 3. Rectangular box around region of interest.

$\theta < \pm 15°$) and $\Delta z = 16\lambda_0$. The number of iterations required at each step as determined using a maximum allowable norm for the error vector of 0.000 58 is plotted in Fig. 2.

Fig. 2 shows that the number of iterations required at each step is small. As range increases the number of iterations per step decreases. This is because the rate of change of the field decreases as the radius of curvature of the beam increases and the phase front tends toward that of a plane wave. This will not occur over irregular terrain, because as the field solution marches forward, new scattered fields will be generated each time the solution passes over a terrain feature. It is possible to reduce the number of iterations per step by reducing the step size, however, the total number of steps is then higher, therefore, no overall gain is achieved. Over irregular terrain the step size is restricted by the gradient of the terrain in the direction of propagation.

III. Nonreflecting Boundary Conditions

Computational calculations in three dimensions can require significant computer resources. Restricting the size of the computational domain to include only the region of interest is an important method for controlling the computational costs. Here the region of interest is enclosed using a nonphysical rectangular box (see Fig. 3). A new nonreflecting boundary condition is imposed on the surface of this box. This boundary condition is now derived and evaluated.

The nonreflecting boundary condition is derived for the upper numerical boundary on the top of the box, but can be easily applied to the sides of the box simply by interchanging the x and y coordinates.

The 3-D PE in the absence of an atmosphere is given by

$$\frac{\partial^2 u}{\partial x^2} + \frac{\partial^2 u}{\partial y^2} + 2jk_0 \frac{\partial u}{\partial z} = 0 \tag{29}$$

where propagation is predominantly along the z axis and x is the vertical axis. Taking a Laplace transform of the 3-D PE with respect to z, we obtain

$$\frac{\partial^2 \hat{u}}{\partial x^2} + \frac{\partial^2 \hat{u}}{\partial y^2} + 2jk_0 p\hat{u} = 0 \tag{30}$$

where the initial field $u(x = H, y, z = 0)$ at the boundary is assumed to be zero. The Laplace transformed 3-D PE of (30) can be expressed using two equations for the x and y components

$$\left(\frac{\partial^2}{\partial x^2} + \Lambda_x^2\right)\hat{u} = 0 \tag{31}$$

$$\left(\frac{\partial^2}{\partial y^2} + \Lambda_y^2\right)\hat{u} = 0 \tag{32}$$

where $\Lambda_x^2 + \Lambda_y^2 = \Lambda_0^2$ and $\Lambda_0^2 = 2jk_0 p$. We can also express Λ_x and Λ_y using

$$\begin{aligned} \Lambda_x &= \cos\phi\Lambda_0 \\ \Lambda_y &= \sin\phi\Lambda_0 \end{aligned}. \tag{33}$$

Equation (31) can be factored into an upward and downward traveling wave component. Discarding the downward traveling component, we arrive at

$$\left(\frac{\partial}{\partial x} - j\cos\phi\Lambda_0\right)\hat{u} = 0. \tag{34}$$

This boundary condition, however, is only valid for a single plane wave, incident on the boundary with azimuth angle ϕ. The boundary condition of (34) can be generalized such that any discrete number of plane waves can be perfectly absorbed.

$$\left[\prod_{q=1}^{Q}\left(\frac{\partial}{\partial x} - j\cos\phi_q\Lambda_0\right)\right]\hat{u} = 0. \tag{35}$$

This expression is the same as the Qth-order generalized impedance boundary condition given by Senior and Volakis [11, eq. (8.22)] applied to the Laplace transformed field. The rigorous derivation of generalized impedance boundary conditions was first performed by Rytov [12] and is reproduced in Senior and Volakis [11]. The Crank–Nicholson scheme [8], used with the 3-D PE, is accurate to second order and, therefore, we restrict the generalized boundary condition to second order for consistency

$$\prod_{q=1}^{2}\left(\frac{\partial}{\partial x} - j\cos\phi_q\sqrt{2jk_0 p}\right)\hat{u} = 0 \tag{36}$$

where ϕ_q are Brewster angles [11]. Material boundaries can possess one or more Brewster angles, depending on whether they exhibit anisotropy or consist of thin layers, etc. For our purposes, we are dealing with a fictitious nonreflecting surface and, thus, we have the freedom of imposing any Q convenient arbitrary Brewster angles. In reality, we would require an infinite number of such Brewster angles to guarantee the exactness of the nonreflecting boundary condition over all incidence angles and, thus, a perfect simulation of free-space. However, a compromise between exactness and computational

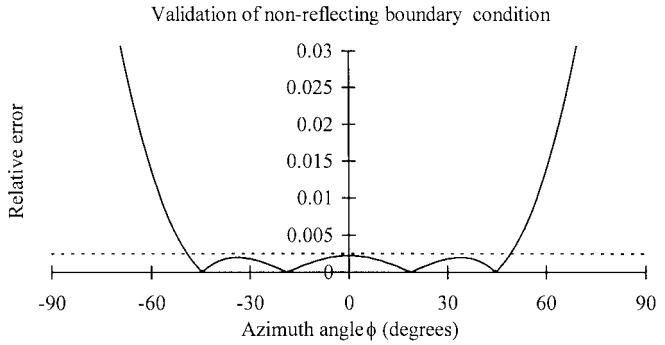

Fig. 4. Three-dimensional PE NRBC ($\theta = 14°$).

effort is to select just two ϕ_q, which is consistent with the second-order accuracy of the PE method itself. The Brewster angles in (36) give a degree of control over the boundary condition. If the angle of incidence is known, values of ϕ_q can be chosen to make the boundary condition exact (within the approximation of the 3-D PE). If the angle of incidence is not known or the incident energy consists of many components with different angles of incidence, near-optimum values of ϕ_q can in principle be selected. These optimum values are chosen such that the boundary condition performs to the level of accuracy implicit in the parabolic equation over the widest possible range of azimuth angles. Equation (36) can be expanded and inverse Laplace transformed to give

$$\frac{\partial u}{\partial x} = \frac{\cos\phi_1 \cos\phi_2 (-1+j)}{\cos\phi_1 + \cos\phi_2} \sqrt{\frac{k_0}{\pi}} \int_0^z \frac{\partial u}{\partial \kappa} \frac{d\kappa}{\sqrt{z-\kappa}} - \frac{j}{(\cos\phi_1 + \cos\phi_2)\sqrt{2jk_0\pi}} \int_0^z \frac{\partial^2 u}{\partial x^2} \frac{d\kappa}{\sqrt{z-\kappa}}. \quad (37)$$

This equation can be descretized and incorporated into the Crank–Nicholson scheme.

Validation of the 3-D PE NRBC is done by substituting a uniform plane wave solution into (36) for various azimuth, ϕ and elevation, θ angles of incidence. The variable p is taken to be a differential operator with respect to z. The error is then given by (38) in terms of the angles θ and ϕ

$$e = \sin\theta\cos\phi - \frac{\cos\phi_1\cos\phi_2}{\cos\phi_1 + \cos\phi_2}\sqrt{2(1-\cos\theta)} - \frac{1}{\cos\phi_1 + \cos\phi_2} \frac{\sin^2\theta\sin^2\phi}{\sqrt{2(1-\cos\theta)}}. \quad (38)$$

Equation (38) is plotted in Fig. 4 and the range of angles over which the boundary condition is valid is assessed. The error introduced by the boundary condition is plotted for an angle of propagation from the z axis set at $\theta = 14°$. This is close to the maximum angle allowable by the narrow angle 3-D PE.

It can be seen in Fig. 4 that the NRBC is valid (error is less than the paraxial approximation of the 3-D PE itself) up to $\pm 50°$. This is achieved with $\phi_1 = 22°$ and $\phi_2 = 45°$. It should be noted that had a smaller value of θ been chosen, the angular domain over which the NRBC is satisfactory would then be larger. The angular limits given above can be thought of as worst-case limits.

A numerical experiment was performed to test the boundary condition in free-space. A Gaussian aperture field with $1/e$ beamwidth of 4.5° was propagated to a distance of $20\,000\lambda_0$ inside a rectangular box whose cross section was $48\lambda_0 \times 48\lambda_0$. In Fig. 5 the root mean square (rms) error across the field plane, compared to the exact analytical solution, is plotted against propagation distance. It can be seen that the nonreflecting boundary condition results in an rms error across the field plane of less than 1 dB up to a distance of $20\,000\lambda_0$. However, it must be noted that the 1-dB rms error bound shown includes both the errors arising from the implementation of the nonreflecting boundary condition as well as the cumulative errors due to the discretization of the 3-D PE method itself.

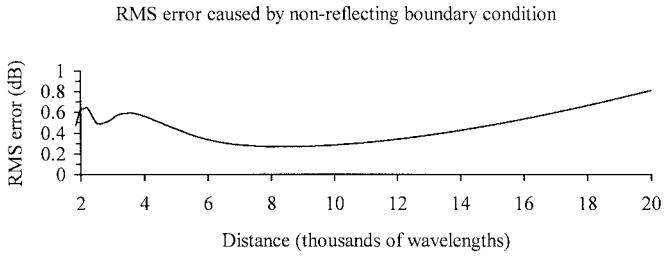

Fig. 5. Gaussian beam propagation in free-space.

The inclusion of the nonreflecting boundary condition into the Crank–Nicholson scheme is straightforward. Because of the flexibility in placing the new boundary condition terms appearing on the diagonal either in matrix $\mathbf{A}$ or $\mathbf{B}$ in (28), the convergence of the iterative algorithm described in Section II can be readily maintained. Thus, the enforcement of the convergence conditions (15) and (16) can be guaranteed. The question of stability of the algorithm after the inclusion of the boundary condition has been found numerically not to pose a problem, as illustrated in the discussion of the previous paragraph and Fig. 5.

IV. Terrain Boundary Condition

At the lower field points, the boundary condition for the air-ground interface must be met. This condition is given by the Leontovich boundary condition, which links the value of the field at the interface to the derivative of the field normal to the surface of the interface

$$\frac{\partial U}{\partial n} = -jk_0\delta U \quad (39)$$

where δ is the normalized surface impedance.

A mathematical derivation of the Leontovich boundary condition is given by Maclean and Wu [13]. The method commonly used to implement the terrain boundary condition for the 2-D PE is that of Levy [14]. This boundary condition is derived by factoring the fast varying phase term out of the Leontovich boundary condition. Substituting the 2-D PE into this gives

$$\sin\theta_g \frac{j}{2k_0}\frac{d^2u}{dx^2} = \cos\theta_g \frac{du}{dx} - \sin\theta_g jk_0 u + jk_0\delta u \quad (40)$$

that can be expressed using finite differences. This boundary condition can then be applied to irregular boundaries as described by Levy, "For upward sloping terrain, one vertical

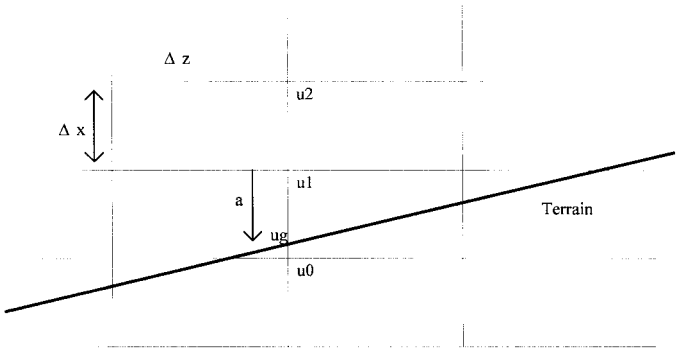

Fig. 6. Virtual field point below the terrain.

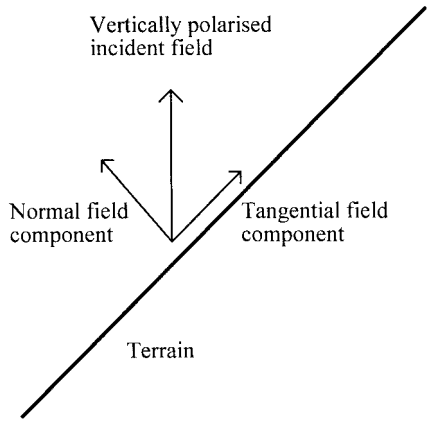

Fig. 7. Field components in transverse plane.

grid point is eliminated at each range step. For downward sloping terrain, one vertical grid point is added at each range step. Since the vertical grid is fixed, the horizontal step size is adapted to the terrain slope, so that the number of vertical grid points is either conserved or increased by ± 1 at each step." This may result in long integration times for complex boundaries.

This approach has been shown to work well in 2-D, however, the terrain surface must coincide with the field points. This condition severely restricts the choice of step size. When the 2-D PE is extended to 3-D, the terrain height is likely to vary across the plane of field points transverse to the direction of propagation, therefore, it will not be possible to meet the above conditions at all points across the field plane. Quantization of the terrain height, such that the terrain surface and the grid points across the field plane coincide is a possible solution. This is seen as crude and is likely to give rise to errors. An alternative approach is to devise a boundary condition that can be used when the terrain surface falls between field grid points. This new boundary condition uses the concept of virtual field points below the terrain surface and is presented below. First, the concept is explained using a 2-D example, then the boundary condition is extended to 3-D.

A. 2-D Virtual Field Points Below the Ground

In this section, a novel method for implementing boundary conditions on terrain that falls between grid points in 2-D is presented.

In Fig. 6, the ground lies between the grid points u_0 and u_1. The field on the ground is given by u_g. The vertical distance between the ground and point u_1 is given by a as a proportion of Δx. The field points u_0, u_1, and u_2 can be expressed as a Taylor series expansion about the field point on the ground u_g. Here they are given in matrix form

$$\begin{pmatrix} u_0 \\ u_1 \\ u_2 \end{pmatrix} = \begin{pmatrix} 1 & -(1-a)\Delta x & \frac{(1-a)^2\Delta x^2}{2} \\ 1 & a\Delta x & \frac{a^2\Delta x^2}{2} \\ 1 & (1+a)\Delta x & \frac{(1+a)^2\Delta x^2}{2} \end{pmatrix} \begin{pmatrix} u_g \\ \frac{\partial u_g}{\partial x} \\ \frac{\partial^2 u_g}{\partial x^2} \end{pmatrix}. \quad (41)$$

The square matrix can be inverted to find the field and its derivatives on the ground in terms of u_0, u_1, and u_2

$$u_g = \left(\frac{a^2+a}{2}\right)u_0 + (1-a^2)u_1 + \left(\frac{a^2-a}{2}\right)u_2 \quad (42)$$

$$\frac{\partial u_g}{\partial x} = \left(\frac{-(1+2a)}{2\Delta x}\right)u_0 + \left(\frac{2a}{\Delta x}\right)u_1 + \left(\frac{1-2a}{2\Delta x}\right)u_2 \quad (43)$$

$$\frac{\partial^2 u_g}{\partial x^2} = \left(\frac{1}{\Delta x^2}\right)u_0 + \left(\frac{-2}{\Delta x^2}\right)u_1 + \left(\frac{1}{\Delta x^2}\right)u_2. \quad (44)$$

These expressions can be substituted into (40) to give an equation that can be incorporated into the Crank–Nicholson scheme and imposes the Leontovich boundary condition on a ground that falls between two grid points.

This method gives a greater degree of control over the selection of the propagation step size. The use of virtual field points below the terrain is believed to be original work. This technique for implementing the lower boundary condition is used in all the 2-D PE predictions presented in this paper mainly because of its flexibility and convenience. We have ascertained that the method of virtual points does not, however, result in any discernible performance advantage or prediction accuracy improvements over Levy's method [14].

Values of δ are given for field components that are normal to the terrain in the transverse plane (vertical polarization in 2-D) and for field components that are tangential to the terrain in the transverse plane (horizontal polarization in 2-D). In three dimensions, there will be terrain gradients that are transverse to the direction of propagation. In this case, assuming the incident energy is vertically polarized there will be a normal field component and a tangential field component in the transverse plane. This is illustrated in Fig. 7, where propagation is into the page.

At the terrain surface, the normal and tangential field components must be found subject to the Leontovich boundary condition using the normal and tangential values of δ, respectively. Since the values of δ are different the ratio of the normal and tangential field components will change, causing depolarization. This is a vector field scattering mechanism and, therefore, cannot be rigorously incorporated into a scalar field propagation model. In order to proceed we must either approximate the boundary condition or extend the parabolic equation method into a vector form.

The assumption made here is that when the terrain gradient in the transverse plane is less than 45°, the normalized impedance for the normal field component alone can be used.

Also, when the terrain gradient in the transverse plane is greater than 45°, the normalized impedance for the tangential component alone can be used. This assumes that the amount of depolarization is small. This assumption is likely to lead to an overprediction of signal strength because the energy being coupled into horizontal polarization is not modeled and, therefore, remains as vertical polarization, giving a larger signal strength prediction. The assumption made is thought to be fairly crude and the development of an effective surface impedance term, which is a function of the transverse terrain gradient forms part of planned further work.

Using the definition of a directional derivative

$$\frac{\partial U}{\partial n} = \underline{\hat{n}} \cdot \underline{\nabla} U. \tag{45}$$

The surface normal unit vector can be written as

$$\underline{\hat{n}} = n_1 \underline{\hat{x}} + n_2 \underline{\hat{y}} + n_3 \underline{\hat{z}} \tag{46}$$

using the surface normal unit vector we can find the surface normal derivative operator to be

$$\frac{\partial}{\partial n} = n_1 \frac{\partial}{\partial x} + n_2 \frac{\partial}{\partial y} + n_3 \frac{\partial}{\partial z}. \tag{47}$$

Also, we can write that

$$U = u(x, y, z) e^{jk_0 z} \tag{48}$$

substituting (47) and (48) into (45) we find that

$$n_1 \frac{\partial u}{\partial x} + n_2 \frac{\partial u}{\partial y} + n_3 \left[\frac{\partial u}{\partial z} + jk_0 u \right] = -jk_0 \delta u \tag{49}$$

substituting the 3-D PE of (1) we obtain

$$n_1 \frac{\partial u}{\partial x} + n_2 \frac{\partial u}{\partial y} + n_3 \left[\frac{j}{2k_0} \left(\frac{\partial^2 u}{\partial x^2} + \frac{\partial^2 u}{\partial y^2} \right) + jk_0 u \right] + jk_0 \delta u. = 0 \tag{50}$$

This is the Leontovich boundary condition for the 3-D PE. In order to incorporate the Leontovich boundary conditions of (50) into a matrix system they must be expressed using finite differences. The method described above allows the terrain height to lie between field grid points and, hence, can be used across the width of the field plane. In the next section this method will be extended for use in 3-D.

B. 3-D Virtual Field Points Below the Ground

In order to implement the Leontovich boundary condition of (50), the field and its derivatives with respect to x and y at the surface of the terrain must be found. Since the field point on the ground lies vertically between two grid points, the field and its derivative, with respect to x, can be found directly using (42) to (44) given above. These equations can be inserted directly into the Leontovich boundary condition equations for the 3-D PE.

The derivatives with respect to y cannot be found directly because the terrain surface lies in between the rows of field points, as shown in Fig. 8. Therefore, the derivatives are found along the rows using finite differences and combined using (42).

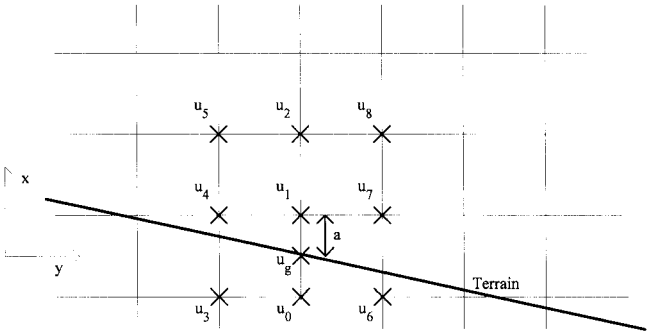

Fig. 8. Field points in transverse field plane (direction of propagation into the paper).

For the first-order derivative in y we use

$$\frac{\partial u_g}{\partial y} = \left(\frac{a^2 + a}{2} \right) \frac{\partial u_0}{\partial y} + (1 - a^2) \frac{\partial u_1}{\partial y} + \left(\frac{a^2 - a}{2} \right) \frac{\partial u_2}{\partial y} \tag{51}$$

where in (51)–(59) the field points are clearly illustrated in Fig. 8 and

$$\frac{\partial u_0}{\partial y} = \left(\frac{-1}{2\Delta y} \right) u_3 + \left(\frac{1}{2\Delta y} \right) u_6 \tag{52}$$

$$\frac{\partial u_1}{\partial y} = \left(\frac{-1}{2\Delta y} \right) u_4 + \left(\frac{1}{2\Delta y} \right) u_7 \tag{53}$$

$$\frac{\partial u_2}{\partial y} = \left(\frac{-1}{2\Delta y} \right) u_5 + \left(\frac{1}{2\Delta y} \right) u_8. \tag{54}$$

Equations (52)–(54) are found from (43), the Δx terms are replaced by Δy terms, and a is set to zero. For the second-order derivative in y we use

$$\frac{\partial^2 u_g}{\partial y^2} = \left(\frac{a^2 + a}{2} \right) \frac{\partial^2 u_0}{\partial y^2} + (1 - a^2) \frac{\partial^2 u_1}{\partial y^2} + \left(\frac{a^2 - a}{2} \right) \frac{\partial^2 u_2}{\partial y^2} \tag{55}$$

where

$$\frac{\partial^2 u_0}{\partial y^2} = \left(\frac{1}{\Delta y^2} \right) u_3 + \left(\frac{-2}{\Delta y^2} \right) u_0 + \left(\frac{1}{\Delta y^2} \right) u_6 \tag{56}$$

$$\frac{\partial^2 u_1}{\partial y^2} = \left(\frac{1}{\Delta y^2} \right) u_4 + \left(\frac{-2}{\Delta y^2} \right) u_1 + \left(\frac{1}{\Delta y^2} \right) u_7 \tag{57}$$

$$\frac{\partial^2 u_2}{\partial y^2} = \left(\frac{1}{\Delta y^2} \right) u_5 + \left(\frac{-2}{\Delta y^2} \right) u_2 + \left(\frac{1}{\Delta y^2} \right) u_8. \tag{58}$$

The derivatives in y can be substituted into the Leontovich boundary condition equation along with the derivatives in x, given in the previous section, to give a finite difference form of the 3-D Leontovich boundary condition. This is in the form

$$g_0 u_0 + g_1 u_1 + g_2 u_2 + g_3 u_3 + g_4 u_4 + g_5 u_5 + g_6 u_6 + g_7 u_7 + g_8 u_8 = 0 \tag{59}$$

and can then be directly inserted into the Crank–Nicholson scheme.

If the transverse terrain gradient is such that the terrain crosses the central row of field points next to the vertical plane of interest, as shown in Fig. 9, left or right finite differences must be used. In Fig. 9 the terrain is sloping from left to right

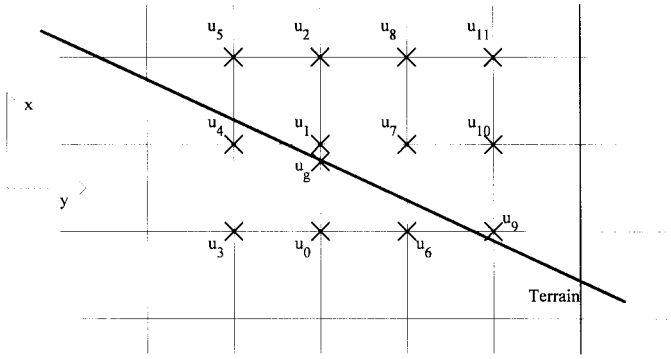

Fig. 9. Calculation of y derivatives using right-hand differences.

causing both the field points u_3 and u_4 to be below the terrain surface. This is not allowed because the number of field points would then be greater than the number of equations leading to an ambiguous solution so field points u_9, u_{10}, and u_{11} are incorporated into a right difference scheme.

Using the method described, the Leontovich boundary condition can be written in terms of nine field points for any transverse gradient. The edges of the field plane are dealt with by using left finite differences at the left-hand side and right finite differences at the right-hand side boundary.

C. Incorporation into Matrix Scheme

It can be seen from Fig. 8 that to implement the Leontovich boundary condition on the terrain surface that lies between field points, requires a square grid of field points. This cannot easily be incorporated into the matrix (28) because each $\mathbf{A}_l$ matrix can only operate on a single column of field points at a time. Likewise, each $\mathbf{B}_m$ matrix can only operate on a single row of field points at a time. In order to proceed, a special method was devised to incorporate the 3-D Leontovich boundary condition into the matrix system. This method is described with reference to Fig. 8. First, the matrix values representing the field points just below the terrain surface in matrix $\mathbf{C}$ in (28) are set to zero. This satisfies the right-hand side of (50). Second, the coefficients related to the field points u_0, u_1, and u_2 are placed at the appropriate row in the $\mathbf{A}_l$ matrix. The coefficients for the field points u_3 and u_6 are placed in the appropriate column in matrix $\mathbf{B}_m$. At this stage the term in $u^{n+1}\{\mathbf{B}_m\}$ is calculated giving us $g_3u_3+g_6u_6$. The term $(g_4u_4+g_5u_5+g_7u_7+g_8u_8)$ is then calculated separately and added directly to the points just below the terrain surface in the matrix $u_{(i)}^{n+1}\{\mathbf{B}_m\}$. The same procedure can be used when left and right finite differences are used.

The comments made at the end of Section III about the convergence of the iterative solver once the 3-D nonreflecting boundary condition has been incorporated also hold for the 3-D terrain boundary condition. The issue of stability (i.e., prediction accuracy) is much more difficult to establish because no canonical solution exists for a nontrivial 3-D terrain boundaries. The simulation results, when compared to the experimental results performed in a controlled laboratory environment (described in Section V), indicate that the iterative algorithm is stable.

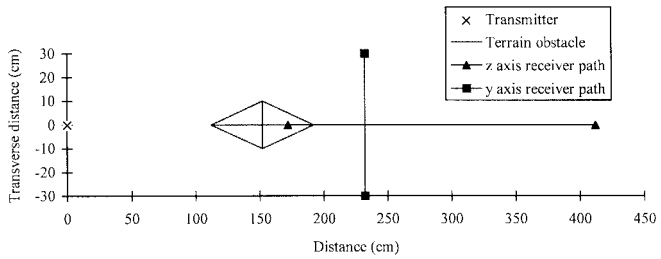

Fig. 10. Terrain obstacle map and receiver paths. Antennas were open-ended WR28 waveguides. Tx height $=$ 0 cm; Rx height $=$ 3.25 cm; Frequency $=$ 30 GHz.

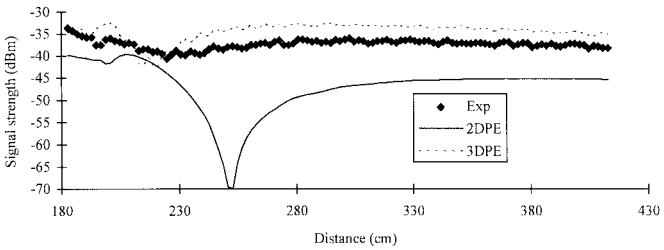

Fig. 11. Indoor propagation measurements and predictions along z axis path (2-D PE mean error 10.64 dB, s.d. 5.61 dBl 3-D PE mean error -1.95 dB, s.d. 1.68 dB).

V. Results

In this section, predictions made by the 3-D PE are compared to propagation measurements. Two sets of measurements were taken; the first in an indoor propagation range at 30 GHz using the principle of scaled frequency modeling. The indoor propagation range provides a controlled idealized environment in which propagation models can be quickly and rigorously validated. In Fig. 10, a pyramidal hill structure of 4.25 cm height is shown along with the transmitter and the receiver paths. The hill structure was made of aluminum and was therefore treated as perfectly conducting. The ground was also a flat aluminum ground plane. Vertical polarization, with one antenna ground-based and the second antenna at a small height above ground level, is used throughout. This represents a worst-case propagation environment in terms of the magnitude of the reflected and diffracted field components. In Fig. 11, measurements taken along the z axis are compared to 2-D PE and 3-D PE predictions. In Fig. 12, measurements along the transverse path are compared to predictions.

It can be seen from Fig. 11 that the 2-D PE underpredicts the signal strength by up to 30 dB. This is because the 2-D PE method treats the pyramid as if it is an infinitely wide wedge, neglecting the diffraction of energy around the sides. The predictions made by the 3-D PE follow the trend of the experimental data very well. The standard deviation for the 3-D PE model 1.68 dB, whereas the standard deviation for the 2-D models is 5.61 dB. There are no large errors present in the predictions made by the 3-D model, as seen in Fig. 11. However, the 3-D PE results show an overprediction of signal strength by approximately 3 dB. This overprediction is due to the fact that depolarization effects caused by the terrain obstacle are not modeled as explained earlier. Depolarization is caused by terrain slopes in the transverse direction causing energy to couple from one vector component of the field (vertical polarization) to another vector component of the

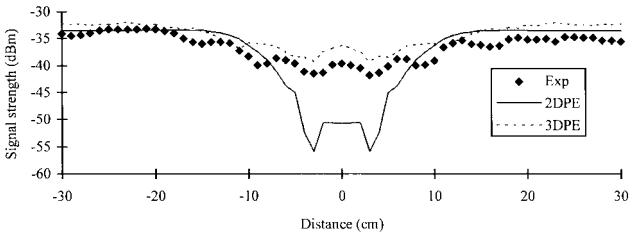

Fig. 12. Indoor propagation measurements and predictions, along y-axis path (2-D PE mean error 1.05 dB, s.d. 4.74 dB; 3-D PE mean error -1.23 dB, s.d 1.05 dB).

field (horizontal polarization). This coupling of vector field components cannot be incorporated into a scalar model such as the current version of the parabolic equation method.

In Fig. 12 the 3-D PE model shows good agreement with the experimental data. Again, there is a small amount of overprediction due to the coupling between vertical and horizontal polarization that is not modeled. In the shadow region there is a large discrepancy between the 2-D models and the experimental data, highlighting the need for 3-D modeling. At distances approaching ± 30 cm from the line of symmetry, the 2-D model gives accurate predictions because the receiver is not in the shadow of the obstacle and, therefore, the direct energy path component dominates.

The second set of measurements were collected in the Bromyard Downs area of Herefordshire, U.K., in the VHF band. Herefordshire was selected for the hilly nature of the countryside. The 10 W of power was transmitted via a disc-cone antenna which was mounted on a 11-m mast. The receiver was vehicle mounted so that measurements could be taken on the move. Measurements were taken at 13-mm intervals, allowing fast fading to be averaged out. The receive antenna was a monopole mounted on the vehicle roof. In Figs. 13 and 14, measurements taken along two routes at 149.875 MHz are compared to 2-D PE and 3-D PE predictions (the horizontal axis is distance along the receiver route *not* distance from transmitter). Terrain height information was obtained from a digital terrain database with a resolution of 50 m. The measurements were taken in cold mildly wet conditions in November 1995 with low atmospheric pressure conditions prevailing throughout. Therefore, the normalized surface impedance values for wet ground [15] were used in all the PE simulations.

Due to computer memory limitations the step size and resolution of the 3-D PE were set at the limit given by Nyquist sampling. The use of the Nyquist sampling values leads to a level of accuracy for the 3-D PE, which is below the optimum achievable due to the additional errors introduced by the finite-difference representation of the PE. Errors due to computer memory limitations are therefore introduced into all the 3-D PE outdoor propagation predictions.

The route corresponding to the results shown in Fig. 13 starts north of the transmitter site and runs south toward the transmitter. It can be seen that the trend in the measurements is predicted by both methods. Underprediction by the 2-D PE method is observed along most of the route. The 3-D PE predictions can be seen to closely follow the predictions of the 2-D PE method along most of the route, however, in the

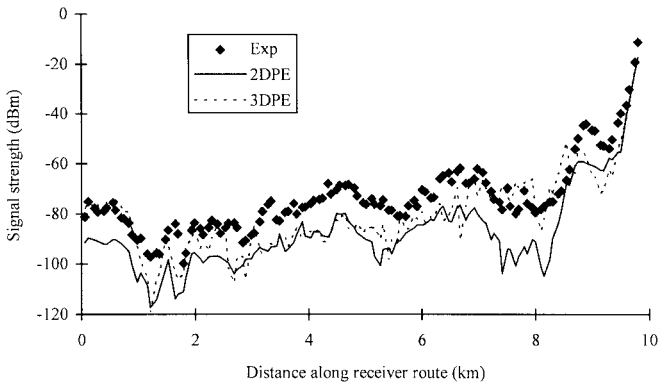

Fig. 13. Propagation predictions and measurements at 149.875 MHz (2-D PE mean error 13.58 dB, s.d. 5.02 dB; 3-D PE mean error 6.76 dB, s.d. 8.34 dB).

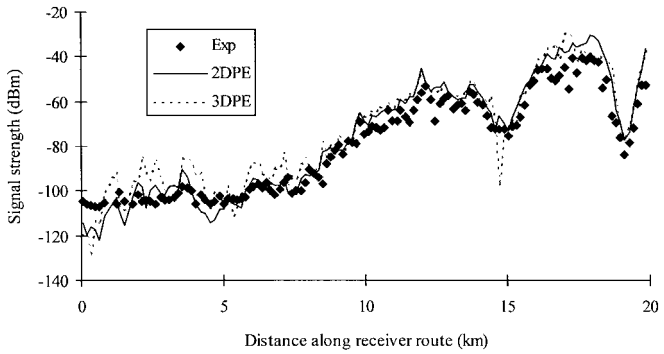

Fig. 14. Propagation predictions and measurements at 149.875 MHz (2-D PE mean error -3.29 dB, s.d. 6.02 dB; 3-D PE mean error -5.41 dB, s.d. 7.33 dB).

region upto 2.5 km and between 7 and 9 km, the 3-D PE method is seen to more accurately predict the level of signal. This is reflected in the mean errors for the route, which are 13.58 dB and 6.76 dB for the 2-D PE and 3-D PE methods, respectively. These results give an indication that improved propagation predictions can be achieved by extending the 2-D parabolic equations to 3-D.

For the case shown in Fig. 14, measurements taken along a 20-km section of road between Leominster and Bromyard (Herefordshire, U.K.) are plotted against the predictions of the 2-D PE and 3-D PE. The mean errors for the 2-D PE and 3-D PE are -3.29 dB and -5.41 dB, respectively, with error standard deviations of 6.02 dB and 7.33 dB. These results are considered to be good. The 2-D PE model has an overprediction of the signal strength of -3.29 dB. This is mainly due to overprediction in the region of 16–19 km, where a line of sight path exists. In Fig. 14, the 3-D PE is seen to closely follow the 2-D PE and the measurements. Spikes can be seen on the 3-D PE plot, these are due to resolution restrictions in the 3-D PE method imposed by the computer memory limitations. This second path corresponds to a much more gently rolling terrain, thus, no significant improvement in going to the 3-D PE method can be observed.

VI. Conclusion

In this paper, the 2-D PE has been extended to 3-D. An efficient iterative solver for the 3-D PE method has been presented. A convergence criterion has been established and

convergence for free-space propagation has been formally proven. The size of the computational domain was constrained to include only the region of interest by placing a nonphysical rectangular box around the region of interest. New nonreflecting boundary conditions are derived, and are imposed on the surfaces of this box. The 3-D terrain surface is incorporated into the 3-D PE method using the concept of virtual field points below the terrain, which is introduced in this paper.

The 3-D PE with these boundaries was used to make predictions for a perfectly conducting 3-D obstacle, which were compared to indoor propagation measurements taken in the University of Birmingham indoor propagation range and predictions made by the 2-D PE. The 2-D PE method was seen to produce significant errors when applied to 3-D environments, however, predictions made by the 3-D PE were seen to be in good agreement with measurements. An overprediction by the 3-D PE of approximately 3 dB was observed. This was caused by depolarization occurring on the transverse terrain gradients that cannot be modeled in the scalar parabolic equation method.

The 3-D PE model was compared to outdoor propagation measurements and predictions made by the 2-D PE were made at 149.875 MHz. The 3-D PE predictions were seen to be in good agreement with both measurements and the 2-D PE predictions. This agreement was achieved despite the restrictions to resolution imposed by our computer memory limitations. In more severe mountainous environments and at a wider range of VHF/UHF frequencies, we have been unable to demonstrate any advantages in going to a 3-D PE method. However, in all these cases we have been severely restricted by the available memory on our computer and these locations were such that far more severe depolarization is expected to occur. The development of a fully 3-D propagation prediction model is thought to be a significant step forward in propagation modeling. This method has been demonstrated to possess good potential for further development.

A 3-D wide-angle PE model has also been developed [16], however, its implementation in realistic scenarios is currently not feasible with current computer technology.

ACKNOWLEDGMENT

The authors would like to thank R. T. Edwards, DERA Malvern, U.K., and B. Freeman, Birmingham University, Birmingham, U.K., for their invaluable assistance in performing the outdoor and indoor measurements, respectively.

REFERENCES

[1] J. H. Causebrook, "Computer prediction of UHF broadcast service area," BBC Res. Rep., vol. RD4, 1974.
[2] J. Walfisch and H. L. Bertoni, "A theoretical model of UHF propagation in urban environments," *IEEE Trans. Antennas Propagat.*, vol. 36, pp. 1788–1798, Dec. 1988.
[3] P. A. Sharples, "The modeling of terrain diffraction phenomena at microwave frequencies," Ph.D. dissertation, Univ. Birmingham, Birmingham, U.K., 1989.
[4] J. S. Finnie, "Prediction of ground-wave propagation over irregular inhomogeneous terrain," Ph.D. dissertation, Imperial College, London, U.K., 1990.
[5] A. E. Barrios, "A terrain parabolic equation model for propagation in the troposphere," *IEEE Trans. Antennas Propagat.*, vol. 42, pp. 90–98, Jan. 1994.
[6] M. D. Collins and S. A. Chin-Bing, "A three-dimensional parabolic equation model that includes the effects of rough boundaries," *J. Acoust. Soc. Amer. (JASA)*, vol. 87, no. 3, 1990.
[7] D. Lee and S. T. McDaniel, "Ocean acoustic propagation by finite difference methods," *Comput. Math. Applicat.*, vol. 14, no. 5, 1987.
[8] J. D. Hoffman, *Numerical Methods for Engineers and Scientists*. New York: McGraw-Hill, 1992.
[9] A. R. Mitchell and D. F. Griffiths, *The Finite Difference Method in Partial Differential Equations*. New York: Wiley, 1980.
[10] C. E. Fröberg, *Numerical Mathematics*. Menlo Park, CA: Benjamin/Cummings, 1985.
[11] T. B. A. Senior and J. L. Volakis, *Approximate Boundary Conditions in Electromagnetics*. Piscataway, NJ: IEEE Press, 1995.
[12] S. M. Rytov, "Calcul du skin-effect par la methode des perturbations," *J. Phys.*, vol. 2, pp. 233–242, 1940 (USSR).
[13] T. S. M. Maclean and Z. Wu, *Radiowave Propagation Over Ground*. London, U.K.: Chapman Hall, 1993.
[14] M. F. Levy, "PE modeling of electromagnetic wave propagation in an inhomogeneous waveguide with irregular boundaries," in *Proc. 1st Int. Conf. Math. Numer. Aspects Wave Propagat. (SIAM)*, Strasbourg, France, 1991, pp. 127–135.
[15] CCIR Recommendations, Int. Telecommunicat. Union, 1992.
[16] C. A. Zelley, "Radiowave propagation over irregular terrain using the parabolic equation method," Ph.D. dissertation, Univ. Birmingham, Birmingham, U.K., 1996.

Chris A. Zelley (S'94–M'97) was born near Bristol, U.K., on March 30, 1968. He received the B.Eng. (electrical and electronics engineering) and the Ph.D. degrees from the University of Birmingham, Birmingham, U.K., in 1989 and 1997, respectively.

From 1989 to 1993, he was engaged in the research and development of receiver systems for direction finding and signal recognition applications. In 1993 he returned to the University of Birmingham to study radiowave propagation. From 1997 to 1998 he worked at the Defence, Evaluation, and Research Agency, Malvern, U.K., designing GaAs monolithic microwave integrated circuits. He is currently a Research Scientist at Bell Laboratories, Lucent Technologies, Swindon, U.K. His current research interests are BiCMOS radio frequency integrated circuit (RFIC) design for global system for mobile communications (GSM) applications.

Costas C. Constantinou (M'91) was born in Famagusta, Cyprus, in 1964. He received the B.S. (electronic and communications engineering) and Ph.D. (electronic and electrical engineering) degrees from the University of Birmingham, U.K., in 1987 and 1991, respectively.

In 1989, he joined the Faculty of the School of Electronic and Electrical, University of Birmingham, U.K., as a full-time Lecturer and, subsequently, as a Senior Lecturer. He currently heads the radio-wave propagation research activity in the Communications Engineering Research Group, Birmingham. His research interests include optics, electromagnetic theory, electromagnetic scattering and diffraction, electomagnetic measurement, radio-wave propagation modeling, mobile radio, and communcations networks.